# Ultrafast atomic view of laser-induced melting and breathing motion of metallic liquid clusters with MeV ultrafast electron diffraction

Jun Wu[a,b,1], Minxue Tang[c,1], Lingrong Zhao[a,b], Pengfei Zhu[a,b], Tao Jiang[a,b], Xiao Zou[a,b], Liang Hong[d,e], Sheng-Nian Luo[c,2], Dao Xiang[a,b,f,g,2], and Jie Zhang[a,b,f,2]

[a]Key Laboratory for Laser Plasmas (Ministry of Education), School of Physics and Astronomy, Shanghai Jiao Tong University, Shanghai 200240, China; [b]Collaborative Innovation Center of IFSA (CICIFSA), Shanghai Jiao Tong University, Shanghai 200240, China; [c]School of Materials Science and Engineering, Southwest Jiaotong University, Chengdu 610000, China; [d]School of Physics and Astronomy, Shanghai Jiao Tong University, Shanghai 200240, China; [e]Institute of Natural Sciences, Shanghai Jiao Tong University, Shanghai 200240, China; [f]Tsung-Dao Lee Institute, Shanghai Jiao Tong University, Shanghai 200240, China; and [g]Zhangjiang Institute for Advanced Study, Shanghai Jiao Tong University, Shanghai 200240, China

Contributed by Jie Zhang; received June 30, 2021; accepted December 16, 2021; reviewed by Aaron Lindenberg and Bradley Siwick

**Under the irradiation of an ultrafast intense laser, solid materials can be driven into nonequilibrium states undergoing an ultrafast solid–liquid phase transition. Understanding such nonequilibrium states is essential for scientific research and industrial applications because they exist in various processes including laser fusion and laser machining yet challenging in the sense that high resolution and single-shot capability are required for the measurements. Herein, an ultrafast diffraction technique with megaelectron-volt (MeV) electrons is used to resolve the atomic pathway over the entire laser-induced ultrafast melting process, from the initial loss of long-range order and the formation of high-density liquid to the progressive evolution of short-range order and relaxation into the metastable low-density liquid state. High-resolution measurements using electron pulse compression and a time-stamping technique reveal a coherent breathing motion of polyhedral clusters in transient liquid aluminum during the ultrafast melting process, as indicated by the oscillation of the interatomic distance between the center atom and atoms in the nearest-neighbor shell. Furthermore, contraction of interatomic distance was observed in a superheated liquid state with temperatures up to 6,000 K. The results provide an atomic view of melting accompanied with internal pressure relaxation and are critical for understanding the structures and properties of matter under extreme conditions.**

ultrafast melting | nonequilibrium state | metallic liquid cluster | ultrafast electron diffraction

An ultrafast laser can induce solid–liquid phase transitions and bring materials into transient states at high temperature and pressure not accessible at equilibrium conditions. The study of the ultrafast melting process under extreme conditions is fundamental to understanding processes such as the atomic pathway in thermal and nonthermal melting, the mechanisms of homogeneous and heterogeneous melting, and the nature of explosive boiling and disintegration of materials. The detailed characterization of such nonequilibrium states in the ultrafast melting process is also important for high-energy-density physics (1, 2).

Strongly driven solid–liquid phase transitions have been extensively studied, and different melting mechanisms have been identified (3–7). Electronic excitations can trigger nonthermal melting for semiconductors and semimetals, usually on a subpicosecond time scale (8, 9). In contrast, metals undergo thermal melting after energy is transferred from electrons to nuclei via electron–phonon scattering (10, 11). With three delocalized electrons, aluminum is a model system for thermal melting studies to validate theoretical models that predict strong ion–ion coupling in the warm dense matter (WDM) regime (12–14). Optical and X-ray spectroscopic methods have been used to investigate the electronic structure and short-range order dynamics in laser-induced melting of aluminum (15–18), but they can only provide indirect information on the atomic-scale structure. The first direct observation of such melting process at the atomic level was based on picosecond electron diffraction (19). However, the temporal resolution in this early experiment is not sufficient to record the melting dynamics. During the past decades, time-resolved X-ray/electron diffraction techniques have been improved both in temporal resolution and source brightness (14, 20–23), which allow one to capture structural evolution during melting through the atomic radial distribution functions (RDFs) (4, 24, 25). Despite numerous studies on the thermal melting, the entire melting process, from the initial loss of long-range order to progressive short-range disordering, remains elusive at the atomic level.

The entire melting process involves ultrafast lattice heating, the density fluctuations, and the development of internal pressure. According to the two-temperature model combined with classical molecular dynamics (TTM-MD) simulations (26, 27), ultrafast melting of a thin metal film is significantly affected by the pressure relaxation process and induced acoustic vibration. While laser-induced pressure is essential for shock-wave and WDM studies (14, 28–30), the local atomic structure

## Significance

**Intense lasers can be used to drive materials into transient states far from equilibrium. Investigations of such states and processes at the atomic scale are of fundamental significance in understanding a material's behavior under extreme conditions. Herein, an ultrafast electron diffraction technique is used to track the atomic pathway of the entire melting process of aluminum and reveal a coherent breathing motion of polyhedral clusters in transient liquid aluminum at high temperature and high pressure. The negative expansion behavior of interatomic distances in a superheated liquid state upon heating is observed. These findings provide insight into ultrafast structural transformations and transient atomic dynamics under extreme conditions.**

Author contributions: D.X. and J.Z. designed research; J.W., M.T., L.Z., P.Z., T.J., and X.Z. performed research; J.W., M.T., L.H., S.-N.L., D.X., and J.Z. analyzed data; and J.W., M.T., S.-N.L., D.X., and J.Z. wrote the paper.

Reviewers: A.L., SLAC National Accelerator Laboratory; and B.S., McGill University.

The authors declare no competing interest.



[1]J.W. and M.T. contributed equally to this work.

[2]To whom correspondence may be addressed. Email: sluo@swjtu.edu.cn, dxiang@sjtu.edu.cn, or jzhang1@sjtu.edu.cn.

This article contains supporting information online at http://www.pnas.org/lookup/suppl/doi:10.1073/pnas.2111949119/-/DCSupplemental.

Published January 24, 2022.

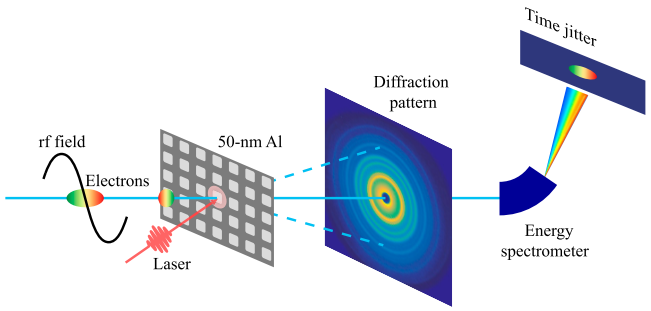


**Fig. 1.** Schematic of the experimental setup. An electron beam is longitudinally compressed with an rf field and then used to probe the laser-excited aluminum. The diffracted beam is measured with a phosphor screen carrying information on the sample's atomic structure, and the undiffracted beam is measured with a downstream energy spectrometer for correcting timing jitter.

(e.g., interatomic distance and coordination numbers [CNs]) of the transient liquid in response to laser-induced compression has been rarely investigated. The evolution of the local atomic structure originates from the redistribution of polyhedral clusters in different liquid states along the melting process, the depiction of which requires high temporal and spatial resolution.

Here, the megaelectron-volt (MeV) ultrafast electron diffraction (UED) with enhanced beam brightness and temporal resolution is employed to track the ultrafast melting process of aluminum and the associated evolution of the local structure of polyhedral clusters in the transient liquid under extreme conditions. Combined with TTM-MD simulations, a comprehensive picture of the coherent breathing motion of clusters during the entire ultrafast transition from solid to short-lived transient liquid of solid density, and finally to long-lived equilibrium liquid in the presence of pressure relaxation is presented. Furthermore, it was observed that high-coordinated clusters in the liquid state with a larger bond length tend to evolve into low-coordinated clusters with a shorter interatomic distance as the temperature increases to 6,000 K in the superheated regime. These results and observations provide an atomic-scale view of ultrafast melting and are critical for understanding the structures and properties of matter under extreme conditions.

## Results

**MeV UED.** The main challenge in studying ultrafast melting is that dramatic changes in structure occur on a subpicosecond time scale, and the sample is damaged after laser excitation, requiring a high-resolution, single-shot capability for measurements. The high resolution is essential to capturing the ultrafast dynamics, and the single-shot capability allows the measurement to be done with a reasonable number of samples. In this experiment, MeV electrons that significantly mitigate the space charge effect (31, 32) are used to record the diffraction patterns

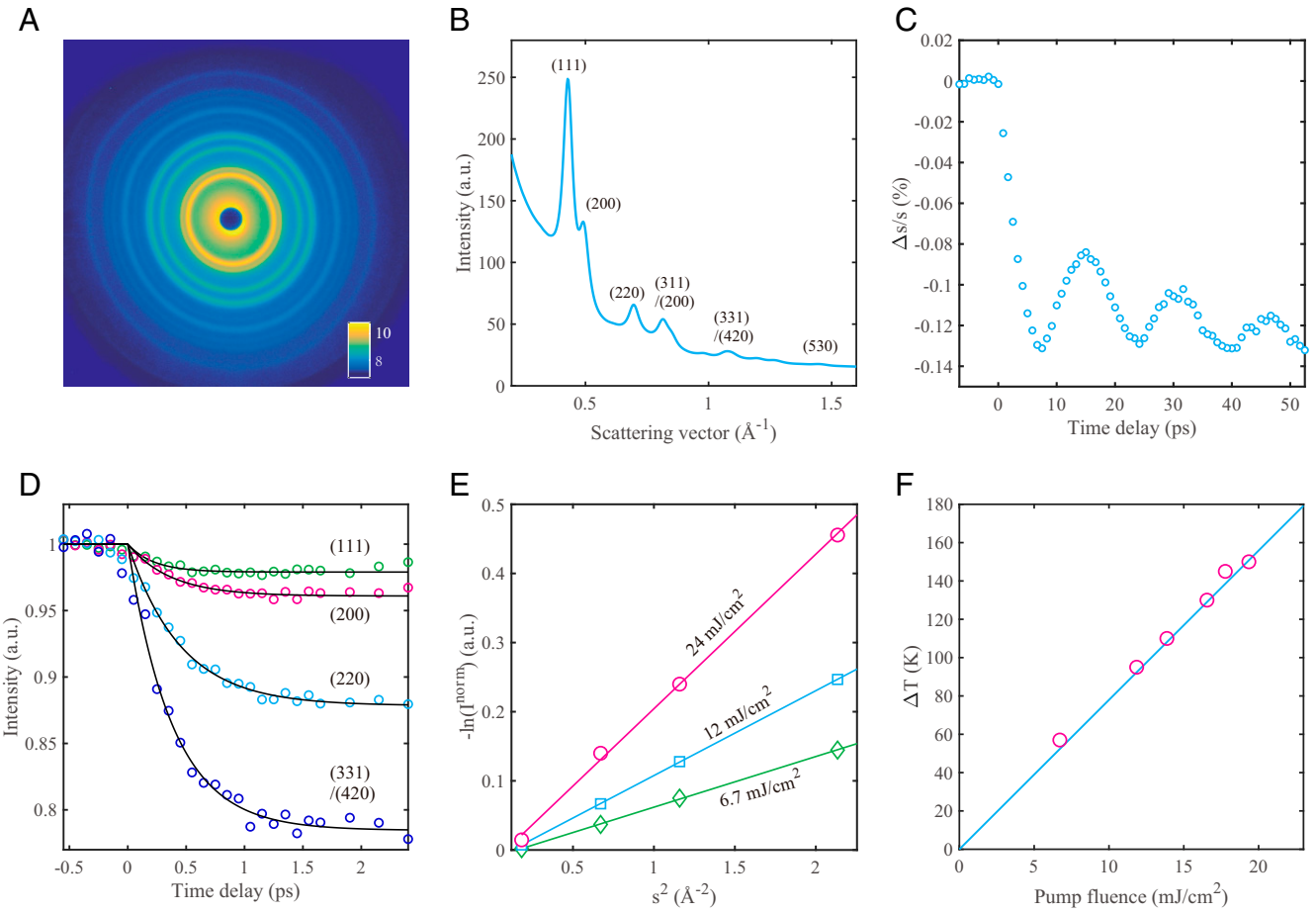


**Fig. 2.** UED data in the reversible regime. (*A*) Raw diffraction pattern taken without laser excitation. (*B*) Corresponding radially averaged distribution. (*C*) Temporal evolution of the position of the Bragg peak (111). (*D*) Temporal traces of the intensity of four selected Bragg peaks (open circles) at an incident fluence of 24 mJ/cm$^2$. Solid lines represent single exponential fits of the data, yielding nearly the same time constants of 0.4 ps. (*E*) Natural logarithm of normalized intensities of four selected peaks as a function of $s^2$. (*F*) Increase in lattice temperature as a function of the incident pump fluence.

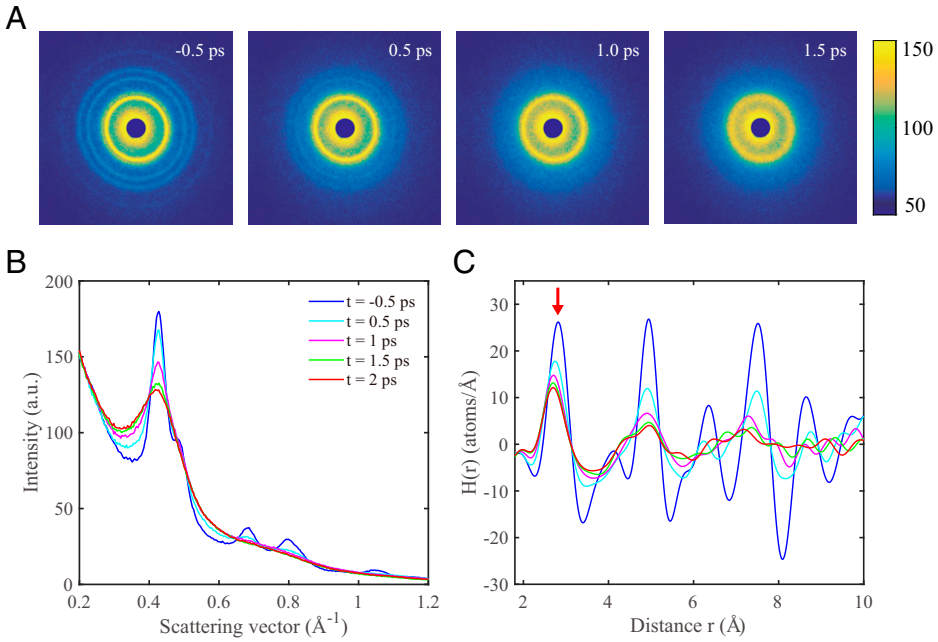


**Fig. 3.** Ultrafast melting of aluminum. (*A*) Snapshots of raw diffraction patterns averaged over 10 shots at various delay times. (*B*) The radially averaged intensity profiles of diffraction patterns. (*C*) RDFs corresponding to the diffraction data in *B*.

in the single-shot mode. Furthermore, the electron beam is compressed by a radiofrequency (rf) cavity, and the timing jitter after compression is corrected by measuring the beam energy for achieving a high temporal resolution (33, 34).

As shown in Fig. 1, when the electron beam passes through the rf cavity at the zero-crossing phase, the electrons at the bunch head are decelerated while those at the bunch tail are accelerated. After a drift, the bunch tail catches up with the bunch head at the position of the sample, leading to bunch compression. As a result, the 3.2-MeV electron pulse with a large bunch charge of about 100 fC is compressed to about 120 fs (full width at half maximum, FWHM) as measured by the THz streaking method (33, 35). Then, a 30-fs (FWHM) 800-nm laser is used to excite the polycrystalline aluminum foil, and the electron scattering patterns are recorded with a phosphor screen. The centroid energy of the electron beam after compression is measured on a shot-to-shot basis to correct the timing jitter introduced during the rf compression process. This is achieved by making a hole in the phosphor screen to allow the undiffracted beam to pass through, and the energy of the transmitted direct beam is measured with a downstream energy spectrometer (34). With this setup, the diffraction pattern and beam energy are measured simultaneously, allowing the timing jitter to be corrected and an overall time resolution of 150 fs (FWHM) to be achieved. It is worth pointing out that the shot-to-shot time jitter also limits the time resolution in X-ray free-electron laser facilities, and a similar "measure and sort" approach has been used to improve the resolution in the pump-probe experiment (36, 37).

**Reversible Dynamics with Laser Heating.** Pump-probe measurements in the reversible regime with laser fluence well below the melting threshold were first performed to obtain the laser heating dynamics of the crystalline state (11). The sample thickness and absorbed energy as a function of incident pump fluence were determined to compare experimental observations and theoretical calculations extended to the irreversible melting regime. Electron diffraction patterns (Fig. 2*A*) accumulated over 50 shots were measured in a transmission geometry, and the radially averaged intensity profile of the Bragg peaks as a function of the scattering vector $s$ ($s = 2\sin\theta/\lambda$) is shown in Fig. 2*B*, where $\theta$ is one half of the scattering angle and $\lambda$ is the wavelength of the electron. The typical diffraction peaks in Fig. 2*B* were fitted to obtain the position (Fig. 2*C*) and intensity (Fig. 2*D*) of the peaks as a function of delay time.

The initial shift of peak positions from 0 ps to 8 ps in Fig. 2*C* originated from the expansion of the aluminum film. The degree of expansion is consistent with the expansion coefficient multiplied by increased temperature (about 60 K) derived from Debye–Waller effect. The oscillatory motion of peak positions in Fig. 2*C* with a period of ~17 ps indicates the propagation of acoustic waves in the polycrystalline aluminum (38, 39). Due to ultrafast heating across the thin film, a newly expanded equilibrium lattice position was established at a speed much faster than the lattice response. Such impulsive and displacive excitation induced a coherent lattice vibration around the new equilibrium position, and stretched and compressed lattice states are alternately reached. The stretching (compression) of the sample leads to the broadening (narrowing) of lattice plane spacing and consequently the contraction (expansion) of the Debye–Scherrer ring radius. The thickness $L$ of the aluminum film is determined to be about 50 nm from the standing wave period of $2L/\nu$, where $\nu$ is the longitudinal sound velocity.

The decay of the diffraction peaks' intensity, as shown in Fig. 2*D*, can be ascribed to lattice heating according to the Debye–Waller model (40):

$$I_{hkl}(t) = I^0_{hkl} \exp\left\{-\frac{4\pi^2}{3} < u^2(t) > s^2\right\}, \quad [1]$$

in which $\langle u^2 \rangle$ is the mean squared atomic displacement that depends on lattice temperature. The dependence of the diffraction intensity on the scattering vector for three representative laser fluences is shown in Fig. 2*E*, where the linear dependence of $-\ln(I^{norm}_{hkl})$ on $s^2$ is in excellent agreement with that predicted in Eq. **1**. The corresponding temperature increase, deduced from slopes in Fig. 2*E* and parameterization of the Debye–Waller factor (41), exhibits a linear relation with the incident pump fluence as shown in Fig. 2*F*. The solid line in Fig. 2*F* gives a linear regression fit of the data, whose slope, $a$, multiplied by the heat

capacity of aluminum, $C_l$, gives the absorbed energy per incident fluence ($aC_l$). From the measurements on reversible dynamics, sample thickness and absorbed energy per incident fluence are determined, enabling quantitative comparison between TTM-MD simulations and experimental observations of the melting process.

**Loss of Long-Range Order in Melting.** As pump fluence is increased above the melting threshold, the aluminum lattice will rapidly destabilize and collapse into disorder. This irreversible transition occurs on the picoseconds time scale and strongly depends on pump fluence. The diffraction patterns at various delay time for 500 mJ/cm$^2$ laser fluence were measured and are shown in Fig. 3*A*. Diffraction patterns with a sufficient signal-to-noise ratio is obtained with integration over just 10 pulses due to the increased beam brightness. As shown in Fig. 3 *A* and *B*, the diffraction rings of solid polycrystalline Al are no longer observable after about 1.5 ps, implying a complete loss of long-range order within 1.5 ps. The melting time is significantly shorter than the 3.5 ps determined with kiloelectron-volt electron diffraction reported previously (4), because of the higher incident laser fluence that leads to higher heating rate and nucleation rate.

In order to investigate the structural evolution during the melting process, the atomic RDF was determined by a sine transform of the diffraction profile in reciprocal space (see *SI Appendix* for additional details). Fig. 3*C* shows the calculated RDF $H(r)$ at five delay times. Before laser irradiation (−0.5 ps), the correlation peaks in $H(r)$ from 2 Å to 10 Å correspond to the characteristic interatomic distance between atoms in the face-centered cubic structure of Al. As the phase transition proceeds, the correlation peaks over 6 Å diminish to noise level rapidly in 1.5 ps, and only short-range correlations in atomic position remain. These observations imply the loss of long-range order during the melting process and the formation of a liquid-like structure. In addition, it is noticeable that the position of the first peak (marked by the red arrow in Fig. 3*C*) in $H(r)$ shows a significant shift to low distance as the height of the peak reduces. Understanding the mechanism for this shift requires RDF analysis on a longer time scale and TTM-MD simulations, as discussed below.

**Ultrafast Short-Range Order Evolution.** Although the ultrafast loss of long-range order and the emergence of a transient liquid state occurred in 1.5 ps, a much longer time was needed to establish a metastable liquid state. The transient liquid state, which is highly unstable, formed immediately after laser melting has a density close to that of solid state (42). The atomic pathway approaching the metastable liquid state of low density from this high-density liquid state is strongly influenced by the progressively short-range disordering and pressure relaxation. Here, by recording scattering signals over a wide momentum transfer range from 0.2 to 1.2 Å$^{-1}$, the evolution of the short-range order, particularly the interatomic distance and CNs, were tracked, revealing a comprehensive picture of the entire melting process. The radially averaged diffraction intensity as a function of the scattering vector recorded from −0.7 to 50 ps is shown in Fig. 4*A*. The experiment involved measurements at 60 time steps, and each data point is integrated over 10 shots with 10 samples to improve the signal-to-noise ratio.

With the benefits of a large momentum transfer range and negligible multiple scattering effects in our MeV-UED measurements, the Bragg peak intensity and diffuse scattering (DS) signal over different scattering regions can be simultaneously observed, providing a complete view of the phase transition dynamics, including long-range disordering and local atomic structure evolution during structural relaxation. Fig. 4*B* compares the temporal evolution of the Bragg peak intensity and DS signal in different scattering regions. As shown in Fig. 4*B*, the increase of the DS intensity at 0.6 Å$^{-1}$ (region b) and the

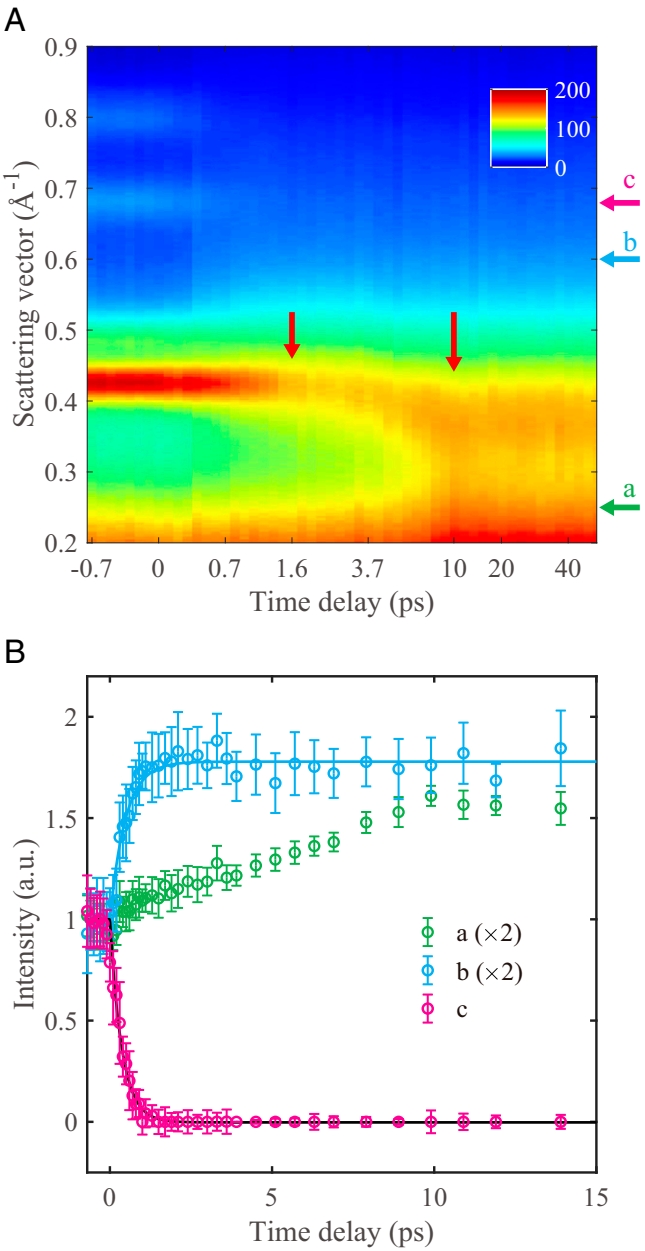


**Fig. 4.** Simultaneous observation of long-range and short-range order. (*A*) Diffraction intensity as a function of time delay and scattering vector. (*B*) Temporal evolution of diffuse scattering intensity in two separate scattering regions (indicated by the arrows labeled as a and b in *A*) and the decay of Bragg peak (220) intensity (indicated by the arrow labeled as c in *A*). The error bar here represents one SD uncertainty.

decay of Bragg peak (220) (region c) exhibit fast dynamics with 1/*e* time constants of 0.6 and 0.4 ps, respectively. Similar time constants are expected because both signals are related to the loss of long-range order. In contrast, the DS intensity at the low scattering vector around 0.25 Å$^{-1}$ (region a) displays slow dynamics with a time scale of about 10 ps. Such nonsynchronous temporal behavior in several scattering vector regions represents dynamics of different length scales. Following the collapse of the lattice a transient liquid state is formed at 1.5 ps, but the structure is far from equilibrium. At longer times up to 10 ps the transient liquid continues to relax, with the main liquid diffraction peak broadening and shifting to a lower scattering vector, as indicated by the red arrows in Fig. 4*A*.

Since the liquid peak width is inversely proportional to correlation length, the result implies that after melting at 1.5 ps the short-range order gradually decreases. The DS intensity evolution in the low scattering vector region hence represents liquid dynamics of short-range order, contributed by the main liquid diffraction peak broadening and shifting. The observed liquid dynamics agree well with the simulated diffraction results based on TTM-MD simulations (*SI Appendix*, Fig. S4). The characteristic time scale of such liquid relaxation dynamics (~10 ps) is consistent with that measured by time-resolved X-ray absorption near-edge spectroscopy (17).

**Relaxation of Pressure Wave and Breathing Motion of Polyhedral Clusters.** The above observations indicate that local structure relaxation plays a vital role in the ultrafast phase transition from solid to metastable liquid. The RDFs were calculated over the whole melting process to explore the short-range order details, and the temporal evolution of the first correlation peak position in RDFs is shown in Fig. 5 *A* and *B*. The temporal evolution of interatomic distance shows three distinctive steps. First, the peak position changes drastically from 2.84 Å to 2.73 Å in the first 2 ps. Second, the peak position moves to a large distance and reaches a maximum excursion of 2.80 Å at about 10 ps. Third, the peak position returns to small distances and reaches a stable value of 2.78 Å at 20 ps.

The CN in the first shell was obtained from RDFs by integrating the area of the first peak, as shown in Fig. 5*A*. The CNs decrease from CN (0 ps) = 12, corresponding to the fcc lattice structure, to CN (2 ps) = 10.5 monotonically and then reaches an equilibrium value of CN (10 ps) = 10. The CNs decrease monotonously during the whole ultrafast melting process. Reduction of CN has been observed for equilibrium metallic melts where the high-coordinated clusters with larger bond lengths transform into low-coordinated ones as the temperature is increased (43). Under a high-temperature condition, atoms with higher kinetic energy tend to break away from high-coordinated polyhedra, resulting in low-coordinated polyhedra with shorter bonding length. Therefore, the radius of the nearest-neighbor shell contracts following the reduction of CNs. However, in the process of ultrafast melting the peak position shifts abruptly to a smaller distance in the first 2 ps and then relaxes back to a larger distance from 2 ps to 10 ps

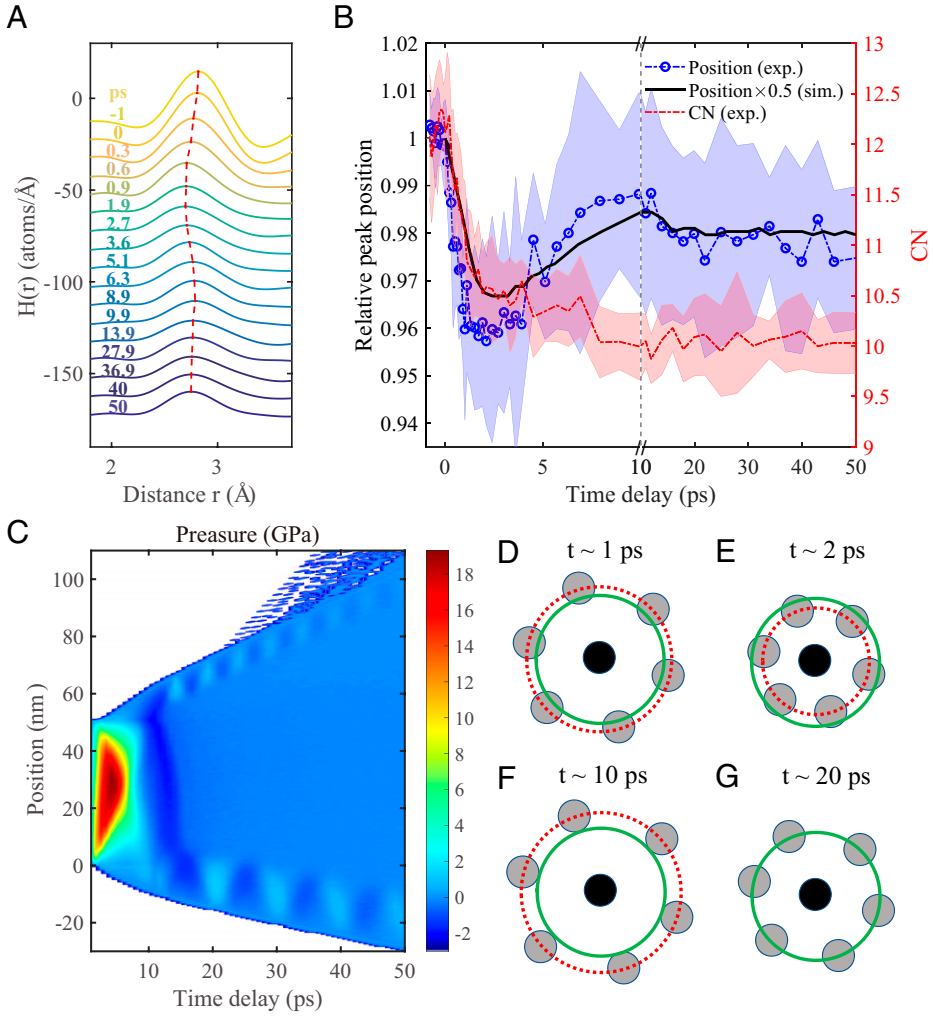


**Fig. 5.** Evolution of local atomic structure in response to pressure wave. (*A*) Experimental $H(r)$ over 1.8 to 3.7 Å. The red dashed line traces the first peak position in H(r). (*B*) The comparison between experimental and simulated evolutions of the first peak position and the evolution of CNs. The blue and red shading area represent error bar (± SD) of peak position and CN, respectively. (*C*) Pressure distribution over the sample as a function of time delay in TTM-MD simulation. (*D*–*G*) Schematic diagram of breathing motion of a polyhedral cluster. The black sphere represents the center atom in a cluster, and gray spheres represent atoms in the first neighbor shell. Red dashed lines indicate the average position of atoms in the first neighbor shell, and for comparison, solid green lines representing the equilibrium position of atoms in the first neighbor shell after 20 ps are plotted in each configuration. The reduction in CN after 1 ps is not displayed in the schematic diagram.

and finally reaches a quasi-steady value after one to two oscillations, highlighting the dynamic effects in this process without an equilibrium counterpart. Considering the transient liquid state at 2 ps, the interatomic distance becomes smaller than that of the equilibrium liquid state after 20 ps while CN is larger, which can be depicted by compressed, high-coordinated polyhedra clusters. On the contrary, in the liquid state at 10 ps, polyhedra clusters are in tension, corresponding to low-CN and larger interatomic distance. The dynamics of the coherent breathing motion of liquid clusters during such a nonequilibrium process can thus be inferred, as illustrated in Fig. 5 *D*–*G*.

To understand the mechanism behind the breathing motion, we examined the local order in the ultrafast melting process with TTM-MD simulation (see *Materials and Methods* for details); the pressure evolution in the Al film is shown in Fig. 5*C*. Local atomic positions during phase transition reproduced by TTM-MD simulations experienced similar oscillations, in reasonable agreement with the experimental observations as shown in Fig. 5*B*. According to simulations (*SI Appendix*, Fig. S6), during the first few picoseconds of ultrafast melting the transient liquid with the density close to solid state is generated prior to hydrodynamic expansion, leading to the first lower minimum at 2 ps in Fig. 5*B*. The transient high-density liquid with a more close-packed structure, corresponding to high CN and low interatomic distance, tends to relax into an equilibrium liquid by expansion. The rapid heating of the lattice and the high-density liquid at the condition of inertial stress confinement gives rise to an initial buildup of compressive pressure in the center of the liquid film. The average compressive pressure in the film reaches a maximum of 12 GPa at 2∼3 ps, corresponding to the time scale to reach the minimum interatomic distance. The subsequent release of the pressure drives the system into an overexpanded liquid state with a longer interatomic distance than equilibrium liquid at about 10 ps, leading to subsequent maximum negative tensile pressure of 3 GPa and upper maximum interatomic distance. The dissipation of stress occurs in the following 50 ps, and finally the metastable liquid state is reached.

**Negative Expansion in Transient Liquid States.** As shown in Fig. 5, after the relaxation of the pressure the sample reaches a metastable liquid state after 50 ps, characterized by reduced CN and shorter interatomic distance than the crystalline state. This metastable liquid state is superheated because the temperature is well above the boiling point. The pump laser fluence was varied from 300 mJ/cm$^2$ to 1,250 mJ/cm$^2$, and high-quality diffraction patterns at a delay time of 50 ps were recorded to study the structure of this superheated metastable liquid state over a wide temperature range. The measured shifts of the first peak in RDFs are shown in Fig. 6.

As shown in Fig. 6, the peak position shows negative shifts to lower interatomic distance with the pump fluence increasing up to 1,250 mJ/cm$^2$, indicating its negative expansion over a wide range of temperatures in the superheated regime. According to the TTM-MD simulation, the maximum temperature of the superheated liquid states was estimated to be about 6,000 K, taking into account the hydrodynamics of the film where the absorbed laser energy was partially transformed into macroscopic kinetic energy. It should be noted that similar negative expansion behavior for the interatomic distance in metallic liquids has been investigated in an equilibrium state but was restricted to a narrow temperature region near the melting point (43). The liquid state of extremely high temperature well above nominal boiling temperature (∼1,450 K at 1 Pa) of aluminum studied in this experiment was not accessible in equilibrium.

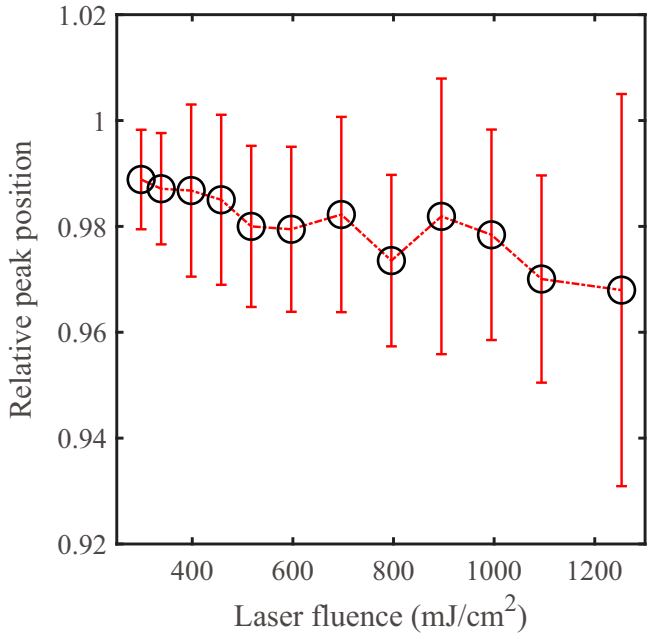


**Fig. 6.** Shift of the first peak in RDFs as a function of laser fluence from 300 to 1,250 mJ/cm$^2$. The error bar here represents one SD uncertainty of relative peak position.

## Discussion

When an ultrafast laser irradiates a substance, most of the incident energy is absorbed by electrons, resulting in an instantaneous increase of electronic temperature within the laser pulse duration. Through electron–phonon coupling, the energy is transferred to the lattice. As the temperature of the lattice increases above the melting temperature, the long-range order is lost following the collapse of the lattice, and only the short-range order survives. In this process, a transient liquid of solid density is first formed, and then compressive pressure is generated due to ultrafast heating and inertial stress confinement. At a longer time scale up to about 20 ps, short-range order and local atomic structure continue to evolve under the influence of pressure relaxation, and a metastable low-density liquid state is finally reached.

Combining high-resolution MeV UED measurements and TTM-MD simulation, an atomic view of the melting process under the effect of laser-induced pressure is achieved through simultaneously recording the evolution of long-range order and short-range order. By tracing the RDFs constructed from the diffraction patterns, the breathing motion of liquid clusters in response to compressive and tensile stress launched by ultrafast heating is resolved. The results indicate a nontrivial melting pathway induced by ultrafast femtosecond laser, compared with a moderate melting process at a much slower heating rate. According to the TTM-MD simulation results, the laser-induced compressive pressure reaches a maximum of about 12 GPa at a 2- to 3-ps delay, and disintegration of the film occurs due to succeeding generation of the tensile stresses. Such a kind of dynamical pressure during ultrafast melting may be utilized to induce liquid–liquid phase transitions (44, 45).

In addition, the contraction of interatomic distance and the reduction of CNs of the first shell upon heating were observed in a wide range of temperature for the transient liquid states. When a disordered liquid state is cooled down through its melting temperature rapidly, the system can be trapped in a local minimum of potential energy surface, and the disordered structure is retained, forming a glassy state. The high-temperature

state before cooling can largely influence the properties of the glassy state. By combining advanced cooling techniques, the superheated liquid state may be transformed into the desired glassy state. The UED measurements herein accompanied by TTM-MD provide an approach to accessing and exploring the disordered materials under a wide range of conditions at the atomic level, which is of great importance for further understanding the properties of the liquids under extreme conditions and the glass transition process (46–48).

## Materials and Methods

**Experimental Details.** The single-shot pump-probe experiments were performed by using rf-compressed MeV UED with the time-stamping technique. The MeV electron pulses were generated in a photocathode rf gun by a 266-nm laser and were further compressed in an rf buncher. The diffracted electrons were recorded by a phosphor screen located 2.7 m away from the sample. The polycrystalline 50-nm aluminum was first deposited onto optically polished NaCl flats by magnetron sputtering and then transferred to an array of 400-μm × 400-μm holes separated by 600 μm on a stainless-steel sheet by conventional floating techniques. The mounted samples were attached to an XYZ-axis motor for target exchange in irreversible measurements. A 30-fs 800-nm laser pumped the samples with a flat-top profile to ensure uniform pumping fluence.

**TTM-MD Simulation Details.** The TTM-MD simulations were conducted for a 50- × 60- × 60-nm$^3$ polycrystalline Al system (~11 million atoms) with the Large-scale Atomic/Molecular Massively Parallel Simulator (LAMMPS) (49–52). The TTM model describes heat transfer through and between electronic and atomic systems. MD models the atomic/ionic system as usual with a molecular dynamics model and the classical force field. Energy can be transferred spatially within the grid representing the electrons and can be transferred between the electronic and the atomic systems. The TTM-MD model equations are given by

$$C_e(T_e)\frac{\partial T_e}{\partial t} = \nabla(\kappa_e \nabla T_e) - g_p(T_e - T_i) + S(t), \quad [2]$$

$$m_j\frac{dv_j}{dt} = -\nabla_j U(r_1, \ldots, r_n) + F_j^{lang}(T_e - T_i) - \frac{\nabla P_e}{n_i}. \quad [3]$$

In Eq. **2** for TTM, $T_e$ and $T_i$ are the electron and ion temperatures, respectively, and $S(t)$ is the absorbed laser pulse intensity with a 30-fs pulse duration. For the 800-nm laser, the absorption rate of laser energy is about 0.13 for aluminum with a 15-nm skin depth (52). For the TTM calculations herein, the $T_e$ dependence of electron heat capacity $C_e$ $(T_e)$ was taken into account and the influence of the electron thermal conductivity $\kappa_e$ was considered. $g_p$ denotes the electron–phonon coupling constant and is related to the energy transfer between electronic and ionic systems. All the parameters used in the TTM simulation are from ref. 52. In Eq. **3** for MD calculations, $m_j$ and $v_j$ are mass and velocity of the $j^{th}$ atom, $U(r_j)$ is the potential energy of the ion system described by the potential, and $F_j^{lang}$ is the random force due to electron–phonon coupling. $P_e$ is electron pressure and $n_i$ is the ion density, which denotes the electron blast force. In this work, the embedded atom method potentials (53) were used to describe the interactions of Al atoms/ions. The coupled Eqs. **2** and **3** are solved with the scheme proposed by Duffy and Rutherford (54, 55).

**Data Availability.** All study data are included in the article and/or supporting information.

**ACKNOWLEDGMENTS.** This work was supported by the National Key R&D Program of China (No. 2021YFA1400202), the National Natural Science Foundation of China (Grant Nos. 11925505, 12005132, 11504232, and 11721091), and the office of Science and Technology, Shanghai Municipal Government (No. 16DZ2260200).



1. A. L. Kritcher *et al.*, Ultrafast x-ray Thomson scattering of shock-compressed matter. *Science* **322**, 69–71 (2008).
2. R. Ernstorfer *et al.*, The formation of warm dense matter: Experimental evidence for electronic bond hardening in gold. *Science* **323**, 1033–1037 (2009).
3. A. Rousse *et al.*, Non-thermal melting in semiconductors measured at femtosecond resolution. *Nature* **410**, 65–68 (2001).
4. B. J. Siwick, J. R. Dwyer, R. E. Jordan, R. J. D. Miller, An atomic-level view of melting using femtosecond electron diffraction. *Science* **302**, 1382–1385 (2003).
5. A. M. Lindenberg *et al.*, Atomic-scale visualization of inertial dynamics. *Science* **308**, 392–395 (2005).
6. G. Sciaini *et al.*, Electronic acceleration of atomic motions and disordering in bismuth. *Nature* **458**, 56–59 (2009).
7. M. Z. Mo *et al.*, Heterogeneous to homogeneous melting transition visualized with ultrafast electron diffraction. *Science* **360**, 1451–1455 (2018).
8. P. Stampfli, K. H. Bennemann, Dynamical theory of the laser-induced lattice instability of silicon. *Phys. Rev. B Condens. Matter* **46**, 10686–10692 (1992).
9. T. Zier, E. S. Zijlstra, A. Kalitsov, I. Theodonis, M. E. Garcia, Signatures of nonthermal melting. *Struct. Dyn.* **2**, 054101 (2015).
10. Z. Lin, L. V. Zhigilei, V. Celli, Electron-phonon coupling and electron heat capacity of metals under conditions of strong electron-phonon nonequilibrium. *Phys. Rev. B Condens. Matter Mater. Phys.* **77**, 075133 (2008).
11. L. Waldecker, R. Bertoni, R. Ernstorfer, J. Vorberger, Electron-phonon coupling and energy flow in a simple metal beyond the two-temperature approximation. *Phys. Rev. X* **6**, 021003 (2016).
12. A. Ravasio *et al.*, Direct observation of strong ion coupling in laser-driven shock-compressed targets. *Phys. Rev. Lett.* **99**, 135006 (2007).
13. B. Nagler *et al.*, Turning solid aluminium transparent by intense soft X-ray photoionization. *Nat. Phys.* **5**, 693–696 (2009).
14. L. B. Fletcher *et al.*, Ultrabright X-ray laser scattering for dynamic warm dense matter physics. *Nat. Photonics* **9**, 274–279 (2015).
15. C. Guo, G. Rodriguez, A. Lobad, A. J. Taylor, Structural phase transition of aluminum induced by electronic excitation. *Phys. Rev. Lett.* **84**, 4493–4496 (2000).
16. M. Kandyla, T. Shih, E. Mazur, Femtosecond dynamics of the laser-induced solid-to-liquid phase transition in aluminum. *Phys. Rev. B Condens. Matter Mater. Phys.* **75**, 214107 (2007).
17. F. Dorchies *et al.*, Unraveling the solid-liquid-vapor phase transition dynamics at the atomic level with ultrafast x-ray absorption near-edge spectroscopy. *Phys. Rev. Lett.* **107**, 245006 (2011).
18. P. M. Leguay *et al.*, Ultrafast short-range disordering of femtosecond-laser-heated warm dense aluminum. *Phys. Rev. Lett.* **111**, 245004 (2013).
19. S. Williamson, G. Mourou, J. C. M. Li, Time-resolved laser-induced phase transformation in aluminum. *Phys. Rev. Lett.* **52**, 2364 (1984).
20. R. P. Chatelain, V. R. Morrison, B. L. M. Klarenaar, B. J. Siwick, Coherent and incoherent electron-phonon coupling in graphite observed with radio-frequency compressed ultrafast electron diffraction. *Phys. Rev. Lett.* **113**, 235502 (2014).
21. S. P. Weathersby *et al.*, Mega-electron-volt ultrafast electron diffraction at SLAC National Accelerator Laboratory. *Rev. Sci. Instrum.* **86**, 073702 (2015).
22. F. Qi *et al.*, Breaking 50 femtosecond resolution barrier in MeV ultrafast electron diffraction with a double bend achromat compressor. *Phys. Rev. Lett.* **124**, 134803 (2020).
23. Y. Xiong, K. J. Wilkin, M. Centurion, High-resolution movies of molecular rotational dynamics captured with ultrafast electron diffraction. *Phys. Rev. Res.* **2**, 43064 (2020).
24. B. J. Siwick, J. R. Dwyer, R. E. Jordan, R. J. D. Miller, Femtosecond electron diffraction studies of strongly driven structural phase transitions. *Chem. Phys.* **299**, 285–305 (2004).
25. M. Mo *et al.*, Visualization of ultrafast melting initiated from radiation-driven defects in solids. *Sci. Adv.* **5**, eaaw0392 (2019).
26. D. Ivanov, L. Zhigilei, Combined atomistic-continuum modeling of short-pulse laser melting and disintegration of metal films. *Phys. Rev. B Condens. Matter Mater. Phys.* **68**, 064114 (2003).
27. D. S. Ivanov, L. V. Zhigilei, Effect of pressure relaxation on the mechanisms of short-pulse laser melting. *Phys. Rev. Lett.* **91**, 105701 (2003).
28. A. Benuzzi-Mounaix *et al.*, Electronic structure investigation of highly compressed aluminum with K edge absorption spectroscopy. *Phys. Rev. Lett.* **107**, 165006 (2011).
29. B. I. Cho *et al.*, Electronic structure of warm dense copper studied by ultrafast x-ray absorption spectroscopy. *Phys. Rev. Lett.* **106**, 167601 (2011).
30. L. Rapp *et al.*, Experimental evidence of new tetragonal polymorphs of silicon formed through ultrafast laser-induced confined microexplosion. *Nat. Commun.* **6**, 7555 (2015).
31. X. J. Wang, D. Xiang, T. K. Kim, H. Ihee, Potential of femtosecond electron diffraction using near-relativistic electrons from a photocathode RF electron gun. *J. Korean Phys. Soc.* **48**, 390–396 (2006).
32. J. B. Hastings *et al.*, Ultrafast time-resolved electron diffraction with megavolt electron beams. *Appl. Phys. Lett.* **89**, 184109 (2006).
33. L. Zhao *et al.*, Terahertz streaking of few-femtosecond relativistic electron beams. *Phys. Rev. X* **8**, 21061 (2018).
34. L. Zhao *et al.*, Noninvasive time-sorting in radio frequency-compressed ultrafast electron diffraction. *Struct. Dyn.* **8**, 044303 (2021).
35. L. Zhao *et al.*, Terahertz oscilloscope for recording time information of ultrashort electron beams. *Phys. Rev. Lett.* **122**, 144801 (2019).
36. D. M. Fritz *et al.*, Ultrafast bond softening in bismuth: Mapping a solid's interatomic potential with X-rays. *Science* **315**, 633–636 (2007).
37. M. Harmand *et al.*, Achieving few-femtosecond time-sorting at hard X-ray free-electron lasers. *Nat. Photonics* **7**, 215–218 (2013).
38. H. Park, X. Wang, S. Nie, R. Clinite, J. Cao, Direct and real-time probing of both coherent and thermal lattice motions. *Solid State Commun.* **136**, 559–563 (2005).

39. J. Li, R. Clinite, X. Wang, J. Cao, Simulation of ultrafast heating induced structural dynamics using a one-dimensional spring model. *Phys. Rev. B Condens. Matter Mater. Phys.* **80**, 014304 (2009).
40. B. E. Warren, "Diffraction by a small crystal" in *X-ray Diffraction* (Dover Publications, 1990), pp. 35–38.
41. H. X. Gao, L. M. Peng, Parameterization of the temperature dependence of the Debye-Waller factors. *Acta Crystallogr. A* **55**, 926–932 (1999).
42. A. M. Lindenberg *et al.*, X-ray diffuse scattering measurements of nucleation dynamics at femtosecond resolution. *Phys. Rev. Lett.* **100**, 135502 (2008).
43. H. Lou *et al.*, Negative expansions of interatomic distances in metallic melts. *Proc. Natl. Acad. Sci. U.S.A.* **110**, 10068–10072 (2013).
44. Y. Katayama *et al.*, A first-order liquid-liquid phase transition in phosphorus. *Nature* **403**, 170–173 (2000).
45. Q. Yu *et al.*, Pressure-induced structural change in liquid GaIn eutectic alloy. *Sci. Rep.* **7**, 1139 (2017).
46. P. G. Debenedetti, F. H. Stillinger, Supercooled liquids and the glass transition. *Nature* **410**, 259–267 (2001).
47. X. Bian, J. Guo, X. Lv, X. Qin, C. Wang, Prediction of glass-forming ability of metallic liquids. *Appl. Phys. Lett.* **91**, 221910 (2007).
48. X. J. Liu *et al.*, Metallic liquids and glasses: Atomic order and global packing. *Phys. Rev. Lett.* **105**, 155501 (2010).
49. S. Plimpton, Fast parallel algorithms for short-range molecular dynamics. *J. Comput. Phys.* **117**, 1–19 (1995).
50. G. E. Norman, S. V. Starikov, V. V. Stegailov, I. M. Saitov, P. A. Zhilyaev, Atomistic modeling of warm dense matter in the two-temperature state. *Contrib. Plasma Phys.* **53**, 129–139 (2013).
51. V. V. Pisarev, S. V. Starikov, Atomistic simulation of ion track formation in $UO_2$. *J. Phys. Condens. Matter* **26**, 475401 (2014).
52. S. V. Starikov, V. V. Pisarev, Atomistic simulation of laser-pulse surface modification: Predictions of models with various length and time scales. *J. Appl. Phys.* **117**, 135901 (2015).
53. X. Y. Liu, F. Ercolessi, J. B. Adams, Aluminium interatomic potential from density functional theory calculations with improved stacking fault energy. *Model. Simul. Mat. Sci. Eng.* **12**, 665–670 (2004).
54. D. M. Duffy, A. M. Rutherford, Including the effects of electronic stopping and electron-ion interactions in radiation damage simulations. *J. Phys. Condens. Matter* **19**, 016207 (2007).
55. A. M. Rutherford, D. M. Duffy, The effect of electron-ion interactions on radiation damage simulations. *J. Phys. Condens. Matter* **19**, 496201 (2007).